Insight into the extremely different catalytic behaviors of asymmetric and symmetric oxygen vacancies for peroxymonosulfate activation

Shan-Shan Liu [a,b], Huifen Fu [a,b,*], Fei Wang [a,b], Yuwei Wei [a,b], Bingxin Meng [a,b], Peng Wang [a,b], Chen Zhao [a,b], Wen Liu [c], Chong-Chen Wang [a,b,*]

[a] Beijing Key Laboratory of Functional Materials for Building Structure and Environment Remediation, School of Environment and Energy Engineering, Beijing University of Civil Engineering and Architecture, Beijing 100044, China
[b] Beijing Energy Conservation & Sustainable Urban and Rural Development Provincial and Ministry Co-construction Collaboration Innovation Center, Beijing University of Civil Engineering and Architecture, Beijing 100044, China
[c] College of Environmental Sciences and Engineering, Peking University, The Key Laboratory of Water and Sediment Sciences, Ministry of Education, Beijing 100871, China

ARTICLE INFO

ABSTRACT

Oxygen vacancies (OVs) play crucial role in peroxymonosulfate (PMS) activation, however, the corresponding catalytic mechanism is ambiguous. Herein, we constructed abundant interfacial asymmetric oxygen vacancies (As-OVs) in OVs-ZnO/Co$_3$O$_4$ that displayed remarkable different catalytic behavior from the symmetric oxygen vacancies (S-OVs) in OVs-CoO$_x$. Specifically, the As-OVs achieved ultra-fast contaminants degradation ($\sim$ 1 min) through both radical attack and electron-transfer process (ETP), while S-OVs exhibited sluggish kinetics for both pathways. Experimental and theoretical analyses revealed that PMS was easily adsorbed on the As-OVs to form PMS* , then ETP immediately occurred once OVs-ZnO/Co$_3$O$_4$ encountered with electron-rich bisphenol A. When electron-poor benzoic acid replaced bisphenol A, the peroxide bond was quickly broken to produce radicals due to the largely polarized PMS* on the asymmetric sites. Conversely, the S-OVs cannot realize rapid removal of both targets because the symmetric sites weakened ETP. This work provides atomic-level insights to understand the catalytic behaviors of OVs.

1. Introduction

The intensification of organic micropollutants from industrial and domestic sources threatens ecological security and clean water supplies [1–3]. Advanced oxidation processes (AOPs) based on peroxymonosulfate (PMS) in wastewater treatment have received considerable attention by virtue of their strong oxidation capacity in a wide pH operation range [4,5]. Although PMS-based AOPs have been extensively studied, there are still some bottlenecks. For example, radical and nonradical pathways have been reported to degrade organic pollutants in PMS-based AOPs [6,7]. Radicals like hydroxyl radical ($^\bullet$OH) and sulfate radical (SO$_4^{\bullet-}$) with large redox potential degrade pollutants non-selectively while nonradicals like electron-transfer pathway tends to selectively remove targets with electron-rich characteristic [8–11]. As to developing new-generation catalysts for the treatment of actual wastewater with complicated constituents, it is especially significant to

accurately control the desired oxidation pathway and to understand the catalytic behavior. However, the structure-property relationship and catalytic mechanism have not been elucidated clearly.

Metal oxide catalysts have been extensively studied in various fields due to their remarkable activity, stability, adjustable structure and low-cost [12]. Wherein, Co$_3$O$_4$-based materials are considered to be one of the most active catalysts for the activation of persulfate [13,14]. In the past few years, various approaches and technologies were adopted to improve the catalytic activities of Co$_3$O$_4$-based materials, including controlling the exposed crystal facets [15], regulating morphology [16] and size [17], constructing defects [18,19], and combining with another metal oxide [20,21].

Constructing heterojunction is an effective strategy to regulate the catalytic performance, in which the interfacial electronic structure is acknowledged as the key. It is traditionally accepted that the strong interaction (e.g. chemical bond) between the heterogeneous interface

---

provides channel for electron transmission and thus boosts the catalytic activity. By comparison, building defects on the interfacial region is more flexible and feasible for the electronic structure control benefited from the asymmetric coordination environment of the interfacial defects. Oxygen vacancies (OVs) are considered as crucial active sites in controlling the catalytic activity due to the optimized electronic properties and newly formed adsorption sites [22–25]. Interfacial OVs are coordinated with different metals and can be called as asymmetric oxygen vacancies (As-OVs, simply expressed as $M_1 \cdots OV \cdots M_2$), giving rise to the uneven charge distribution [26,27]. Compared with symmetric oxygen vacancies (S-OVs, denoted as $M_1 \cdots OV \cdots M_1$), the As-OVs with local polarized electronic feature will more easily strengthen the adsorption as well as polarization of PMS molecule, enabling the high-efficiency PMS-based AOPs more feasible [28]. Recently, Song et al. proved that the As-OVs with the structure of $Co \cdots OV \cdots Ce$ was beneficial to both the peroxide bond breakage to generate $SO_4^{\bullet-}$ and the desorption of $SO_4^{\bullet-}$, accelerating atrazine (ATZ) degradation [29]. Zhan's group reported that the As-OVs coordinated to Cu and In led to a side-on PMS adsorption mode, and the uneven electron distribution accelerated the electron transfer from As-OVs sites to adsorbed PMS, thus facilitating the cleavage of peroxide bond to produce radicals ($SO_4^{\bullet-}$ and $^\bullet OH$) for tetracycline removal [28]. Although As-OVs have been demonstrated to improve the catalytic activity greatly, the catalytic mechanism is not fully understood. Moreover, the precise control of the desired oxidation pathway by OVs still remain elusive even controversial [29–32], which deserves depth exploration.

Metal-organic frameworks (MOFs) are considered as ideal sacrificial templates to synthesize metal oxides due to the characteristics of adjustable porous structure, controllable composition and easy functionalization [33,34]. Compared with the single-component metal oxide, the mixed metal oxides with rich heterogeneous interfaces will be more prone to lattice distortions and formation of defects, resulting in more As-OVs. Bimetallic MOFs with uniform distribution of metal elements throughout the whole particles are beneficial to the formation of dense interfaces for the derived mixed metal oxides, which will facilitate the production of interfacial As-OVs and the improvement of catalytic activity.

Herein, ZnCo-ZIF as the most reported typical bimetallic MOFs was selected as the template to construct $OVs\text{-}ZnO/Co_3O_4$ containing asymmetric $Zn \cdots OVs \cdots Co$ sites by a glucose-assisted pyrolysis method for PMS activation to degrade contaminants. It was found the distinct behavior between the As-OVs in $OVs\text{-}ZnO/Co_3O_4$ and the S-OVs in OVs-ZnO as well as $OVs\text{-}CoO_x$. The As-OVs with $Zn \cdots OV \cdots Co$ structures were demonstrated as the crucial active sites and enhanced the BPA removal kinetic by about 13 times in comparison to the S-OVs with $Co \cdots OV \cdots Co$ structures. More importantly, the rapid switch from ETP pathway to radical pathway drove by As-OVs was observed when the target was changed from BPA to BA, while very slowly occurred with great difficulty in S-OVs involved systems. Experimental and theoretical analyses revealed the "easy come, easy go" and "easy come, not easy go" behavior induced by As-OVs and S-OVs, respectively. As-OVs anchored PMS molecules to form the PMS* complex, and BPA with electron-rich characteristic donated electrons to form a rapid ETP pathway, while peroxide bond was quickly broken to produce radicals when BPA was replaced by the electron-poor pollutant BA. Conversely, S-OVs in OVs-ZnO and $OVs\text{-}CoO_x$ did not perform well both in ETP and radical pathways owning to their symmetric structures of the OVs. These results give an atomic perspective to understand the relationship among OVs, PMS activation process, target pollutant removal and oxidation pathway, which could guide rational design of Fenton-like catalysts for organic pollutants removal.

2. Materials and methods

2.1. Chemicals and reagents

$Co(NO_3)_2 \cdot 6\ H_2O$, benzoic acid (BA), 4-nitrobrnzoic acid (NBA), Methyl phenyl sulfoxide (PMSO), Methyl phenyl sulfone ($PMSO_2$), D_2O and KI were obtained from Shanghai Macklin Biochemical Co.,Ltd. 2-methylimidazole (2-MI), bisphenol A (BPA), peroxymonosulfate (PMS), 4-Hydroxybenzoic acid (HBA), sulfamethoxazole (SMX), ciprofloxacin (CIP), phenol (PE), atrazine (ATZ), furfuryl (FFA) and 2,2′-bipyridyl (BPY) were purchased from J&K Scientific Company. Methanol and ethanol were purchased from Fuchen (Tianjin) Chemical Reagent Co., Ltd. D-Glucose, NaOH and H_2SO_4 were supplied by Beijing Chemical Reagent Factory, China. NaCl, NH_4HCO_3, NaH_2PO_4, $NaNO_3$, Na_2SO_4 and 1,10-phenanthroline were purchased from Sinopharm Chemical Reagent Co., Ltd. *p*-benzoquinone (*p*-BQ) and $Zn(NO_3)_2 \cdot 6\ H_2O$ were obtained from Aladdin Co. Ltd., China and Tianjin Guangfu Fine Chemical Research Institute, respectively.

2.2. Catalyst preparation

The preparation procedures of ZnCo-ZIF, ZIF-8 and ZIF-67 were described in Supporting Information **Text S1**. The $OVs\text{-}ZnO/Co_3O_4$ was obtained by calcining ZnCo-ZIF as a self-sacrificial template with the assistant of glucose, as shown in Fig. S1. Specifically, 300 mg ZnCo-ZIF and a specific mass of glucose were mixed well and then transferred into a crucible with a cover. After calcination at 550 ℃ for 2 h in a muffle furnace, $OVs\text{-}ZnO/Co_3O_4\text{-}0$ (ZnO/Co_3O_4), $OVs\text{-}ZnO/Co_3O_4\text{-}1$, $OVs\text{-}ZnO/Co_3O_4\text{-}2.5$ and $OVs\text{-}ZnO/Co_3O_4\text{-}5$ ($OVs\text{-}ZnO/Co_3O_4$) (the number represents the mass ratio of glucose to ZnCo-ZIF) were obtained. For comparison, ZnO, OVs-ZnO, Co_3O_4 and $OVs\text{-}CoO_x$ were also prepared by the similar procedure using mono-metal ZIFs like ZIF-8 and ZIF-67 as precursors. The measurements of characterization are described in **Text S2-S4**.

2.3. Catalytic experimental procedure

A certain amount of catalyst was dispersed into a 50 mL target pollutant solution, and then PMS with a specific concentration was introduced to trigger the AOPs reaction. At given time intervals, 1.5 mL liquid samples were withdrawn and filtered by a 0.22 μm PTFE filter, immediately quenched with 10.0 μL methanol, and then detected by HPLC with a C-18 column (2.1 mm × 100 mm, 1.7 μm). The quenching experiments were conducted by adding various different quenching agents including *p*-BQ (10 mM), EtOH (200 mM), FFA (10 mM) and PMSO (1 mM) to determine the role of $O_2^{\bullet-}$, $^\bullet OH + SO_4^{\bullet-}$, $^1O_2$ and high-valent cobalt-oxo, respectively. Relevant analytical testing methods and processes are shown in Table S1 and **Text S5** and **S6**. To determine the practical application potential of the catalyst, the treatment of the actual airport wastewater was carried out. The water quality parameters of the actual airport wastewater (inorganic ion concentration and chemical oxygen demand) are shown in Table S2. The original airport wastewater was diluted by 15 times for the following experiments since its COD concentration (excess 1000 mg/L) is too high and difficult to effectively explain the practical application effect. The COD measurement method is shown in **Text S7**.

3. Results and discussion

3.1. Characterization

The PXRD patterns (Fig. S2a) of ZIF-8, ZIF-67, and ZnCo-ZIF matched well with the simulated ones. As shown in Fig. S2b, the bands at 585 nm and 540 nm belong to tetrahedral coordinated Co(II) in UV–visible diffuse reflectance spectrum of the ZnCo-ZIF suggested the doping of Co(II) into the framework of ZIF-8 [35]. The uniform

distribution of Zn and Co in the same crystal of the ZnCo-ZIF (Fig. S2c) indicated that a solid solution of ZIF-8 and ZIF-67 rather than the physical mixture was formed [35].

ZnO and Co_3O_4 were obtained by annealing ZIF-8 and ZIF-67, respectively (Fig. S3a and S3b). Notably, compared with Co_3O_4 directly derived from ZIF-67, two new weak peaks with heart symbol (♥) at 42.40° and 61.52°, matching well with the (200) and (220) crystal planes of CoO, appeared for the OVs-CoO_x obtained by the glucose-assisted pyrolysis of ZIF-67 (Fig. S3b). This could be attributed to the introduction of OVs those led to the generation of low valence Co^{2+} ions [36]. The XRD patterns (Fig. S3c) of the ZnO/Co_3O_4, OVs-ZnO/Co_3O_4-1, OVs-ZnO/Co_3O_4-2.5 and OVs-ZnO/Co_3O_4 retained all the feature peaks of ZnO, and other three peaks with plum blossom symbol (♣) at 44.81°,

59.36° and 65.24° corresponding well to the (400), (511) and (440) crystal planes of Co_3O_4. It was noteworthy that the characteristic peaks of Co_3O_4 became weaker with the increase of glucose percentage, and almost disappeared for the OVs-ZnO/Co_3O_4, which was likely caused by the lattice defects induced by OVs [37]. Although the content of Co was much lower than that of Zn (Fig. S4), no obvious shift of the XRD peaks after the introducing of Co species ruled out the lattice doping of Co into ZnO (Fig. S3d) [38].

The OVs-ZnO/Co_3O_4 exhibited an irregular spheroid shape with diameters ranging from 50 to 70 nm (Fig. S5a). Very clean-looking lattice fringes were observed, in which the interplanar spacings of 2.4753 Å and 4.6670 Å were corresponded to the (101) plane of ZnO and (111) plane of Co_3O_4 respectively (Fig. S5b). The most distinct and vital diffraction
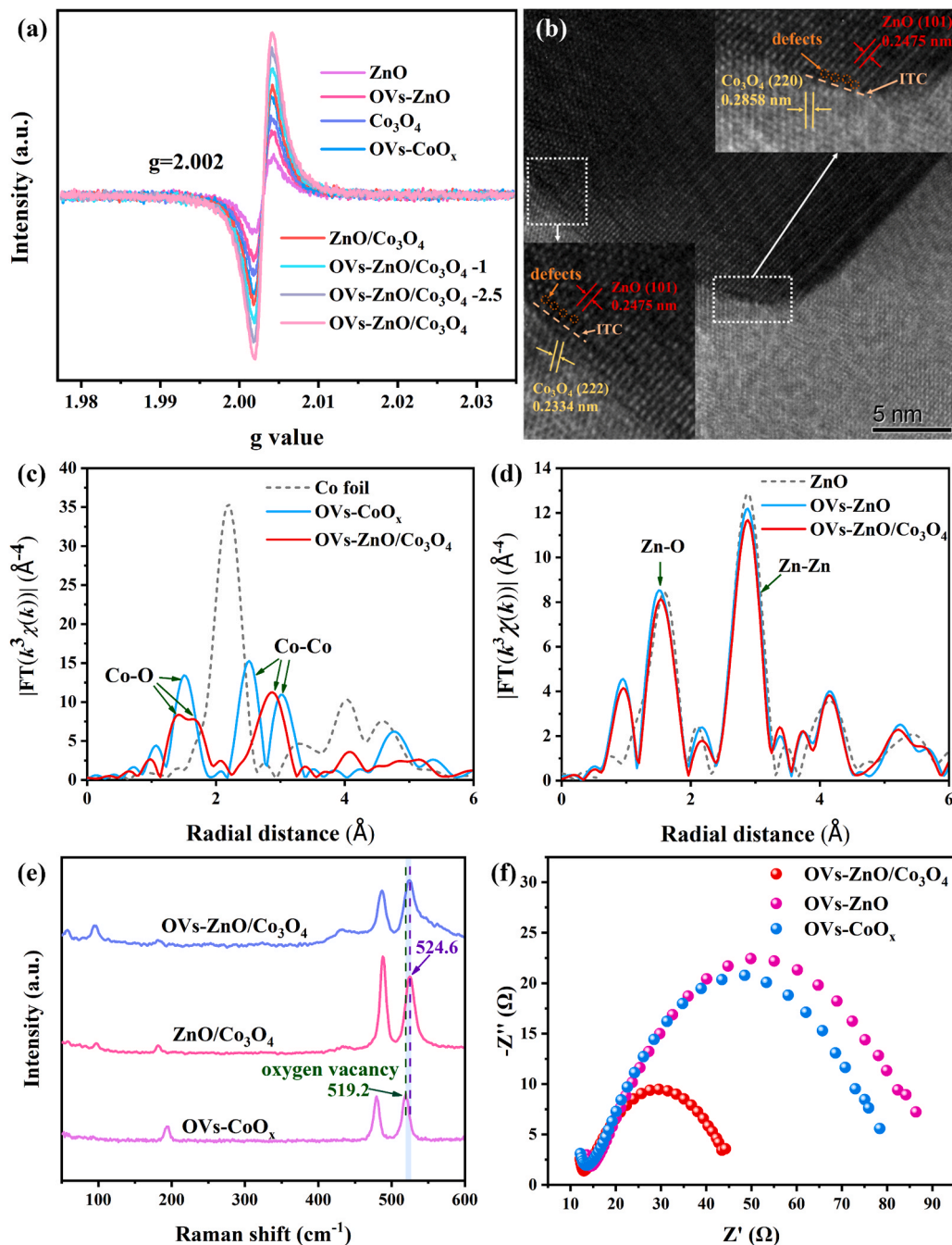

Fig. 1. (a) EPR spectra of all prepared catalysts. (b) HRTEM images of OVs-ZnO/Co_3O_4. FT-EXAFS signals of the (c) Co k-edge and (d) Zn k-edge for OVs-CoO_x, OVs-ZnO/Co_3O_4, OVs-ZnO and their reference samples. (e) Raman spectra of the OVs-CoO_x, ZnO/Co_3O_4 and OVs-ZnO/Co_3O_4 samples. (f) Electrochemical impedance spectroscopy analysis of OVs-CoO_x, OVs-ZnO and OVs-ZnO/Co_3O_4 samples.

patterns in selected-area electron diffraction (SAED) image could also be allocated to the (102) plane of ZnO and (422) plane of Co_3O_4 in the OVs-ZnO/Co_3O_4. Elemental mappings of OVs-ZnO/Co_3O_4 (Fig. S5c) confirmed the well-distribution of elements Zn, Co and O. These results verified the appearance of dense interfaces between ZnO and Co_3O_4, which was crucial to the formation of the interfacial OVs and improvement of catalytic performance.

3.2. Characterization of interfacial As-OVs

The EPR signals with g = 2.002 corresponding to OVs appeared, and all the ZnO/Co_3O_4 composites exhibited stronger signal intensities than the ZnO and Co_3O_4, indicating the easier formation of OVs at heterogeneous interfaces and thus leading to the production of As-OVs (Fig. 1a and Table S3) [39,40]. Consistent with previous studies [41,42], HRTEM (Fig. 1b) and HAADF-STEM images (Fig. S6) indicated that lattice distortions and defects at the interface between ZnO and Co_3O_4 crystals could be attributed to interfacial As-OVs. To further confirm the formation of As-OVs, the coordination information of Co in the

OVs-CoO$_x$ and OVs-ZnO/Co_3O_4 samples and Zn in the OVs-ZnO and OVs-ZnO/Co_3O_4 samples was determined by extended X-ray absorption fine structure spectroscopy (EXAFS) [43,44]. The Co k-edge and Zn k-edge EXAFS signals of all samples were shown in Fig. S7. The characteristic bands of Co-O shell and Co-Co shell appeared in the ranges of 1.2–2.1 Å and 2.5–3.3 Å (Fig. 1c), respectively, while the bands of Zn-O shell and Zn-Zn shell were located in the ranges of 0.8–2.3 Å and 2.5–3.3 Å (Fig. 1d), respectively. The peak intensities of Co-O first shell and Zn-O first shell in the OVs-ZnO/Co_3O_4 were both lower than those in the OVs-CoO$_x$ and OVs-ZnO, respectively, suggesting a decrease in the coordination number [45,46]. To further confirm the change of coordination number, data fitting analysis were conducted (Fig. S8), and the structural information of the catalysts was generalized in Table S4.

The OVs-CoO$_x$ and OVs-ZnO samples exhibited lower coordination numbers (4.2 ± 0.5 and 3.4 ± 0.7 for the Co-O shell and Zn-O shell, respectively) in comparison with the standard Co_3O_4 (5.8 ± 0.4) and ZnO (4.0 ± 0.2), indicating that glucose-assisted pyrolysis facilitated the formation of OVs. Interestingly, compared with OVs-CoO$_x$ and OVs-ZnO samples, OVs-ZnO/Co_3O_4 presented decreased coordination numbers
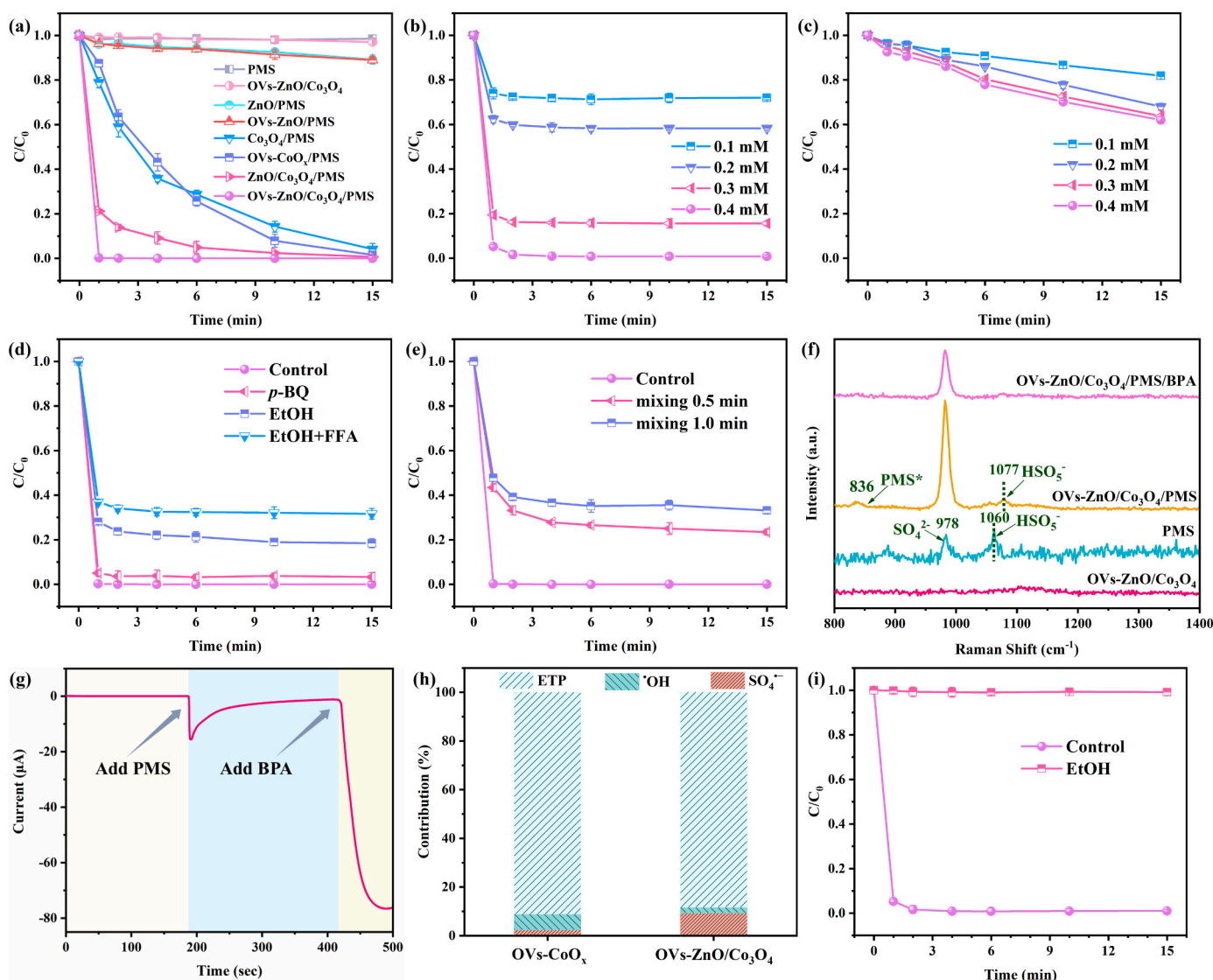

Fig. 2. (a) BPA removal in various systems with 0.1 mM PMS. (b, c) Influence of PMS dosage in BA removal in the (b) OVs-ZnO/Co_3O_4/PMS and (c) OVs-CoO$_x$/PMS system. The ROS quenching tests for (d) BPA and (i) BA removal in the OVs-ZnO/Co_3O_4/PMS system. (e) BPA degradation after mixing 0.1 mM PMS and OVs-ZnO/Co_3O_4. (f) Raman spectra of different processes. (g) i-t curve of OVs-ZnO/Co_3O_4. (h) contribution of $SO_4^{\bullet-}$, $^{\bullet}OH$ and ETP in BPA oxidation in OVs-ZnO/Co_3O_4/PMS and OVs-CoO$_x$/PMS system. Reaction conditions: contaminants concentration = 10 mg/L, catalyst = 0.2 g/L, [PMS]$_0$ = 0.1–0.4 mM, as for quenching tests, [PMS]$_0$ = 0.1 mM for (d) and 0.4 mM for (i), [p-BQ] = 10 mM, [EtOH] = 100 mM, and [FFA] = 10 mM.

(1.6 ± 0.3, 2.3 ± 0.4 and 3.1 ± 0.8 for the Co−O$_I$ shell, Co−O$_{II}$ shell and Zn-O shell, respectively). These results verified that the OVs content was significantly different in the three samples. The different locations of the Co-O shells implied that the dramatically different coordination environments of Co-O in the OVs-ZnO/Co$_3$O$_4$ and OVs-CoO$_x$, thus further proving the existence of As-OVs (Zn···OVs···Co) in OVs-ZnO/Co$_3$O$_4$.

The Raman peak of the OVs-CoO$_x$ at 519.2 cm^{-1} corresponding to OVs shifted to a higher frequency (524.6 cm^{-1}) with the introduction of Co (Fig. 1e) [38]. which could be attributed to the different local environment of OVs in the OVs-CoO$_x$ and OVs-ZnO/Co$_3$O$_4$. It was reasonably speculated that OVs exhibited a symmetric structure (Co···OVs···Co) in the OVs-CoO$_x$ while an asymmetric structure (Zn···OVs···Co) in the OVs-ZnO/Co$_3$O$_4$. Electrochemical impedance spectroscopy (EIS) characterization was carried out to further clarify the intrinsic activity of As-OVs. As shown in Fig. 1f, OVs-ZnO/Co$_3$O$_4$ showed a much smaller semicircular than the OVs-CoO$_x$ and OVs-ZnO, indicating its lower charge-transfer resistance, faster electron transfer rate and thus potential intrinsic catalytic activity.

3.3. Catalytic performance in PMS activation

As shown in Fig. 2a and Fig. S9a, BPA was almost not degraded in the PMS solution without catalyst, and the BPA adsorption was not obvious for all the as-prepared catalysts. ZnO and OVs-ZnO exhibited little BPA degradation abilities due to their typical irreducible characteristic [47]. Co$_3$O$_4$ and OVs-CoO$_x$ presented similar catalytic performance despite their different OVs content. It was noteworthy that k values of the ZnO/Co$_3$O$_4$ is 3.54 times that of the OVs-CoO$_x$ (Fig. S9a) although these two catalysts possessed similar OVs contents (Table S3). Surprisingly, 99.7% BPA was quickly removed in the OVs-ZnO/Co$_3$O$_4$/PMS suspension within just 1 min. These results suggested that the coordination environment rather than concentration of OVs alone determined the intrinsic catalytic activity of catalysts.

In addition, the removal rates k_{obs} of BPA corresponding to the unit oxygen vacancy content of various catalysts were calculated, which was denoted as "M" (the calculation process was observed in **Text S8**) to normalize the catalytic activities of different catalysts for better comparison. As shown in Fig. S9b, the M values of the bicomponent catalysts (ZnO/Co$_3$O$_4$ and OVs-ZnO/Co$_3$O$_4$) were much higher than those of single-component catalysts (ZnO, OVs-ZnO, Co$_3$O$_4$ and OVs-CoO$_x$). This affirmed that catalysts with As-OVs exhibited higher catalytic activities than those of catalysts only containing S-OVs, which was consistent with the EIS results.

To further confirm the conspicuous activity and universality of the OVs-ZnO/Co$_3$O$_4$, several contaminants with different vertical ionization potential (VIP), including BPA, SMX, PE, ATZ, BA, and NBA, were chosen as the target contaminants. However, it was found that the catalytic efficiencies of OVs-ZnO/Co$_3$O$_4$ toward different targets were dramatically different (Fig. S9c), in which nearly 100% of low VIP pollutants such as BPA and SMX were removed with 0.1 mM PMS, while only 30% and 5% of BA and NBA with electron withdrawing groups such as carboxyl and nitro groups (high VIP) were removed, respectively. The above results indicated that OVs-ZnO/Co$_3$O$_4$ had selectivity for removing pollutants with different VIPs, in which the VIPs of pollutants were negatively correlated with removal rates k_{obs} (Table S5). Also, the removal efficiencies of BA (generally considered as a radical probe) and NBA were relatively low, proving that the BPA degradation would not be a radical process [11,48]. It was interestingly observed that the degradation of BA as a radical probe occurred within the first 1 min, and no BA was degraded with prolonging the reaction time, which might be originated from the lack of PMS considered that the molar ratio of PMS to BA was only 1.2. As expected, BA was completely removed within 1 min when the PMS dosage increased to 0.4 mM (Fig. 2b), indicating the rapid formation of radicals in the OVs-ZnO/Co$_3$O$_4$/PMS system. As shown in Fig. S10a-**b**, the leaching Co ions during the reaction process were lower than the standard value (GB 25467–2010) [49], which had

almost no effect on the degradation efficiency during the reaction process (Fig. S10c-**d**). Besides, in a mixed solution of BPA and BA, BPA was firstly removed, and then BA by the OVs-ZnO/Co$_3$O$_4$ (Fig. S9d). Since the catalytic behavior of OVs-ZnO/Co$_3$O$_4$ in the degradation of BPA and BA was significantly different, we believed that different oxidation pathways appeared in removing different targets. In contrast, the OVs-CoO$_x$/PMS system exhibited much lower oxidation rates (Fig. S9e and S11). Especially, OVs-CoO$_x$ could not remove BA effectively even with 0.4 mM PMS (Fig. 2c), meaning the difficulty production of radicals in the OVs-CoO$_x$/PMS system, which was dramatically different from the OVs-ZnO/Co$_3$O$_4$. These distinct catalytic behaviors between the OVs-ZnO/Co$_3$O$_4$ and OVs-CoO$_x$ could be attributed to their different structure features like As-OVs.

3.4. Identification of PMS activation mechanism in BPA and BA

The quenching tests were implemented to distinguish the contribution of different ROS participated in the catalytic oxidation process [48]. Only small decreases occurred in the OVs-ZnO/Co$_3$O$_4$/PMS/BPA and OVs-CoO$_x$/PMS/BPA systems by adding EtOH (Fig. 2d and Fig. S12), implying that both SO$_4^{\bullet-}$ and $^{\bullet}$OH could play negligible role in BPA removal [50]. To further check the role of SO$_4^{\bullet-}$ and $^{\bullet}$OH, the catalytic experiment was conducted in a mixed solution of BPA and BA (Fig. S13). It could be seen that BPA was rapidly removed while BA (generally considered as a radical probe) was hardly eliminated although the reaction rate constants of these two targets with radicals (SO$_4^{\bullet-}$ and $^{\bullet}$OH) were similar (Table S6). This implied that BPA degradation would not be dominated by radicals (SO$_4^{\bullet-}$ and $^{\bullet}$OH).

The BPA removal efficiency was slightly further decreased when both EtOH and FFA were added, which might be attributed to the action of ^{1}O$_2$ [51]. To further verify the role of ^{1}O$_2$, D$_2$O was used as the solvent for BPA degradation because ^{1}O$_2$ lives more than 10 times longer in D$_2$O than it does in H$_2$O [52]. The contribution of ^{1}O$_2$ might be negligible since BPA degradation efficiency was not improved by replacing H$_2$O with D$_2$O (Fig. S14a), and the slight decrease in efficiency was attributed to the atomic exchange effect between the H atom in the hydroxyl group of PMS and D$_2$O [53]. Moreover, the role of ^{1}O$_2$ was further verified through the characteristic ESR signals from TEMP-^{1}O$_2$ adducts. As shown in Fig. S14b, the ESR signal of TEMP-^{1}O$_2$ in OVs-ZnO/-Co$_3$O$_4$/PMS increased after changing the solvent from H$_2$O to D$_2$O, but remained almost unchanged with BPA addition. Similar result was also found for the OVs-CoO$_x$/PMS (Fig. S14c). This affirmed that the ^{1}O$_2$ in the OVs-ZnO/Co$_3$O$_4$/PMS and OVs-CoO$_x$/PMS systems made negligible contribution to BPA degradation. Furthermore, the degradation efficiency of BPA was almost unaffected by the addition of p-BQ (O$_2^{\bullet-}$ scavenger) (Fig. 2d and Fig. S12). However, it was reported that BQ could activate PMS to remove pollutants [54,55], but only 8% of BPA removal efficiency was observed in the p-BQ/PMS system, indicating that the effect of p-BQ on catalytic performance could be eliminated (Fig. S15a). The above experimental results demonstrated that the role of O$_2^{\bullet-}$ in the reaction could be excluded. As shown in Fig. S15b, the extremely weak ESR signal of DMPO–O$_2^{\bullet-}$ indicated that O$_2^{\bullet-}$ hardly participated in BPA removal [56]. The dissolved oxygen was also ruled out due to the maintained catalytic performance after introduction of nitrogen pumping (Fig. S16). As depicted in Fig. S17, PMSO probe method proved that the high-valent cobalt-oxo also played a minor role in BPA removal for both the OVs-ZnO/Co$_3$O$_4$ and OVs-CoO$_x$ [57].

To delve the ETP mechanism in BPA oxidation, PMS and OVs-ZnO/Co$_3$O$_4$ were premixed in advance and then BPA was added after specific time intervals. Since the ETP pathway experienced electron transfer form pollutants to the catalyst, premixing OVs-ZnO/Co$_3$O$_4$ and PMS would not steer obvious effect on contaminant degradation [58]. As shown in Fig. 2e, after premixing 0.5 min and 1 min, the BPA degradation efficiency was decreased by only 23.4% and 33.2%, respectively. Moreover, the residual PMS was nearly zero at 1 min (Fig. S18a), proving that PMS was absorbed on the surface of the OVs-ZnO/Co$_3$O$_4$

rather than being decomposed. The minor inhibitive effect of premixing indicated that ETP regime would dominate in BPA oxidation. Similar results were also observed in the OVs-CoO$_x$/PMS/BPA system (Fig. S18b and c).

Raman spectra (Fig. 2f) was employed to demonstrate the interaction between the OVs-ZnO/Co$_3$O$_4$ and PMS to form a superficial complex PMS* . The 978 and 1060 cm^{-1} peaks were ascribed to SO$_4^{2-}$ and HSO$_5^-$, respectively. A new peak at position 836 cm^{-1} was observed in the OVs-ZnO/Co$_3$O$_4$/PMS system, reflecting the prolonged O-O bond of the adsorbed PMS [59]. The HSO$_5^-$ peak red-shifted from 1060 to 1077 cm^{-1} when OVs-ZnO/Co$_3$O$_4$ was added in comparison with PMS alone, probably because the electron density of S-O bond induced originated from electron transfer between OVs-ZnO/Co$_3$O$_4$ and PMS [60]. After BPA was added into the OVs-ZnO/Co$_3$O$_4$/PMS system, the 836 cm^{-1} and 1077 cm^{-1} peaks disappeared, which could be ascribed to that BPA consumed the absorbed PMS* via an electron transfer pathway. Besides, the PMS* was also formed on the OVs-CoO$_x$, as proved in Fig. S19a. The i-t curve (Fig. 2g) showed the current almost not changed with PMS addition, while significantly decreased after introduction of BPA, suggesting that the electron transfer occurred between the PMS* and BPA [56,61,62]. Similar trend was also observed for the OVs-CoO$_x$ (Fig. S19b).

Co XPS spectra in OVs-ZnO/Co$_3$O$_4$ remained basically unchanged after BPA oxidation (Fig. S20a and Table S7), which indicated that Co^{2+} would not be the key active site for BPA removal and radial pathway would not dominate in BPA degradation. Furthermore, the relative contributions of radicals and nonradicals indicated that ETP rather than radicals played a dominant role in BPA removal (Fig. 2h). The detailed calculation process was given in **Text S9** and **S10** [11,62].

As depicted in Fig. 2i and Fig. S21, the addition of EtOH led to large inhibition of BA degradation both in the OVs-ZnO/Co$_3$O$_4$/PMS and OVs-CoO$_x$/PMS system, indicating that SO$_4^{\bullet-}$ and $^\bullet$OH were the dominated ROS for BA abatement in these two systems. As depicted in Fig. S22, both OVs-ZnO/Co$_3$O$_4$/PMS and OVs-CoO$_x$/PMS system exhibited noticeable signals of DMPO−$^\bullet$OH and DMPO−SO$_4^{\bullet-}$ adducts. Fig. S23 and S24 showed that the OVs-ZnO/Co$_3$O$_4$/PMS system had much more radicals than that in the OVs-CoO$_x$/PMS system. The concentrations of SO$_4^{\bullet-}$ and $^\bullet$OH in the former system reached their maximum within one minute and did not change over time, while were gradually accumulated as the reaction proceeds in the later one, which was consistent with the BA removal efficiency (Figs. 2b and 2c). Details of the quantitative determination of the SO$_4^{\bullet-}$ and $^\bullet$OH were described in **Text S11** and **S12**. Moreover, Fig. S20b and Table S7 showed that the Co^{2+} content decreased while Co^{3+} increased, suggesting that Co^{2+} played a certain role in BA oxidation and thus radials involved in BA removal. Based on the above results, it could be summarized that BA and BPA removal were dominated by two different mechanisms in both OVs-ZnO/Co$_3$O$_4$/PMS and OVs-CoO$_x$/PMS system: ETP-controlled BPA oxidation and radicals-controlled BA degradation.
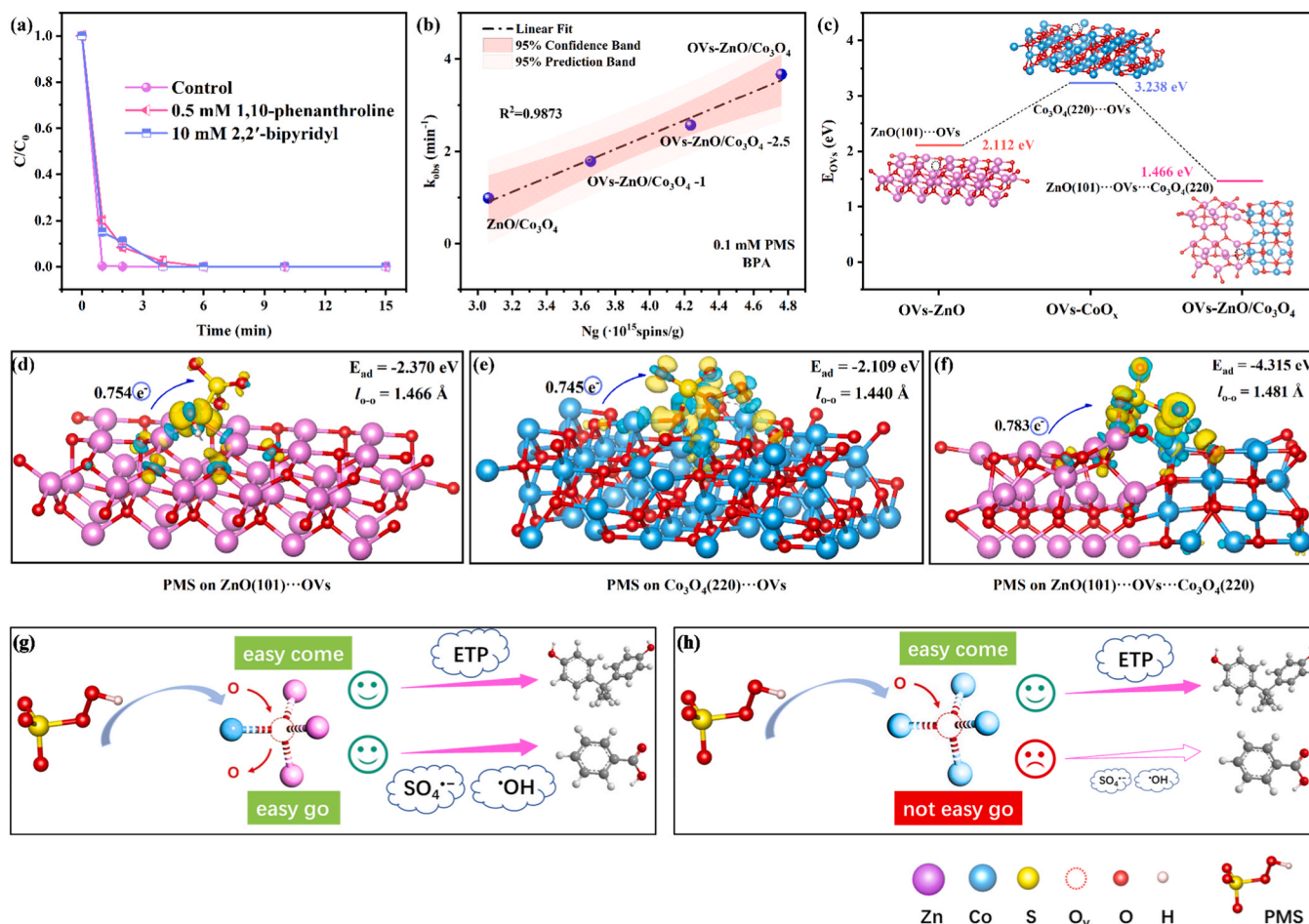

Fig. 3. (a) BPA degradation in the OVs-ZnO/Co$_3$O$_4$/PMS system with 0.5 mM 1,10-phenanthroline and 10 mM 2,2′-bipyridyl for Co^{2+}. (b) Correlation of k_{obs} to OVs content on the BPA removal in OVs-ZnO/Co$_3$O$_4$/PMS system with 0.1 mM PMS. (c) The calculated OVs formation energy in different models. Charge density difference, PMS adsorption energies, O–O bond length of PMS and the number of electron transfer of (d) OVs-ZnO(101)/PMS, (e) OVs-CoO$_x$(220)/PMS and (f) OVs-ZnO (101)/Co$_3$O$_4$(220)/PMS systems. Schematic diagram of catalytic mechanism of (g) As-OVs and (h) S-OVs. Reaction conditions: [OVs-ZnO/Co$_3$O$_4$]$_0$ = 0.2 g/L, [BPA]$_0$ = 10 mg/L, [PMS]$_0$ = 0.1 mM.

3.5. Probing the active sites and DFT calculation for the mechanism analysis

Both metal sites like Co^{2+} and non-metallic sites like OVs are generally considered as the active sites for PMS activation. To identify the actual active sites, metal site masking experiments were conducted. Metal site masking is an effective strategy to verify whether it plays a role in the reaction [63,64]. As shown in Fig. 3**a** and Fig. S25, the BPA removal efficiency in the OVs-ZnO/Co$_3$O$_4$/PMS and OVs-CoO$_x$/PMS systems did not change significantly by masking Co sites using 1,10-phenanthroline and 2,2′-bipyridyl as chelating agents, confirming that the surface Co species were not the active sites.

In addition, the role of OVs in the reaction can also be determined by the S^{2-}/O^{2-} anion exchange strategy [65]. OVs-ZnO/Co$_3$O$_4$ was immersed in Na$_2$S·9 H$_2$O solutions of different concentrations to exchange O^{2-} with S^{2-} to form sulfurized OVs-ZnO/Co$_3$O$_4$. As depicted in Fig. S26, the BPA degradation efficiency was greatly decreased to 0% after immersed in 0.01 M and 0.1 M Na$_2$S·9 H$_2$O solutions in OVs-ZnO/Co$_3$O$_4$/PMS system, indicating that OVs would be the main active sites.

To confirm the role of OVs in BPA and BA removal, the quantitative structure-activity relationship was investigated. Fig. 3**b** showed that the OVs content (Table S3) was positively correlated with the BPA degradation rate (Fig. S27), and the correlation coefficient R^2 was as high as 0.9873. Fig. S28 also showed a good linear relationship between the BA removal rate and the OVs content with the R^2 of 0.9818. These results demonstrated that OVs were the dominated active sites for PMS activation to remove both BPA and BA.

Furthermore, M values of the series bicomponent catalysts were further calculated to better confirm their catalytic activities. As shown in Fig. S29, the different M values of the series bicomponent catalysts could be contributed to that the OVs contents obtained from EPR quantitative data covered both major As-OVs and minor S-OVs. The M value gradually increased with the increase of the amount of glucose used during the annealing process for the series bicomponent catalysts. This could be attributed to that the higher amount of glucose led to the higher As-OVs content, in which the As-OVs would possess the vast majority of the total OVs. The above results indicated that catalysts with higher As-OVs content exhibited higher catalytic activities.

DFT calculations were carried out to further clarify the origin of the excellent catalytic activity and special catalytic behavior of the OVs-ZnO/Co$_3$O$_4$ with As-OVs (**Text S13**). As shown in Fig. S30a-**b** and Fig. 3**c**, the energy to form an oxygen vacancy was 2.112 eV in the ZnO-(101) surface and 3.238 eV in the Co$_3$O$_4$-(220) surface. Interestingly, the formation energy of an oxygen vacancy at the interface of ZnO-(101) and Co$_3$O$_4$-(220) was 1.466 eV, which was much lower than the individual ones, indicating the As-OVs at heterogeneous interfaces were easier to form [66]. Thus, more OVs were produced in the OVs-ZnO/Co$_3$O$_4$ than those in the ZnO and Co$_3$O$_4$, which was corresponding well with the ESR results. Fig. S30c and Fig. 3**d-f** showed that the free energy for PMS adsorption (ΔE_{ads}) was calculated to be $-$ 2.370 eV, $-$ 2.109 eV and $-$ 4.315 eV on the ZnO, Co$_3$O$_4$ and ZnO/Co$_3$O$_4$, respectively. The smaller ΔE_{ads} value of the As-OVs with Zn···OVs···Co structures than that of the S-OVs with Co···OVs···Co and Zn···OVs···Zn indicated the stronger PMS adsorption on the As-OVs [67].

The peroxide bond of the chemically absorbed PMS was extended (*lo*-o $= 1.466, 1.440$ and 1.481 Å in the OVs-ZnO/PMS, OVs-CoO$_x$/PMS and OVs-ZnO/Co$_3$O$_4$/PMS systems, respectively) compared to the free PMS (*lo*-o $= 1.434$ Å) (Fig. 3**d**). This proved that the peroxide bond in PMS was the most unstable one for the As-OVs (OVs-ZnO/Co$_3$O$_4$) compared to that in S-OVs (OVs-CoO$_x$ and OVs-ZnO), making it easier to form OVs-ZnO/Co$_3$O$_4$-PMS* complexes with a higher oxidation potential and also easier to promote the breakup of the peroxide bond to form radicals (SO$_4^{•-}$ and $^•$OH). Meanwhile, it could be seen from Fig. 3**d-f** that electron accumulated around O atoms of PMS, and the overall charge gained of PMS was 0.754, 0.745 and 0.783 for the OVs-ZnO, OVs-CoO$_x$ and OVs-

ZnO/Co$_3$O$_4$, respectively. PMS obtained the most electrons from the OVs-ZnO/Co$_3$O$_4$, indicating the most tendency of the cleavage of peroxide bond to generate radicals [68].

Based on the above experiments and DFT calculation results, it could be concluded that the As-OVs as the active sites enhanced the adsorption and activation of PMS. The O atoms in the PMS were easily adsorbed to the OVs site (easy come) to form OVs-ZnO/Co$_3$O$_4$-PMS* . BPA (electron donor) donated electrons to PMS* directly to be oxidized mediated by OVs-ZnO/Co$_3$O$_4$ as the electron bridge, which would result in a ETP regime for BPA degradation. When BA as an electron-poor target replaced BPA, the As-OVs sites also served as critical active sites to enhance the peroxide bond cleavage of PMS (easy go), rapidly generating radicals (SO$_4^{•-}$ and $^•$OH) and efficiently degrading refractory BA (Fig. 3**g**). The ΔE_{ads} value of the S-OVs was $-$ 2.109 eV, indicating the easy adsorption of PMS (easy come), but the ΔE_{ads} value was much higher than that of As-OVs (-4.315 eV), resulting in a slower rate of BPA removal. Moreover, the length of peroxide bond in PMS adsorbed on S-OVs was much lower than that on As-OVs, bringing about the difficult breaking of peroxide bond in PMS* adsorbed on S-OVs (not easy go), and thus could not effectively generate radicals (SO$_4^{•-}$ and $^•$OH) to remove BA (Fig. 3**h**). Therefore, the As-OVs in the OVs-ZnO/Co$_3$O$_4$ realized both rapid ETP and radial-dominated pathway for the BPA and BA within 1 min, respectively. Conversely, OVs-CoO$_x$ possessed lower reaction rates for the removal of the two organics, in which radicals were difficult to be generated and thus only little BA was degraded even with a high PMS dosage (0.4 mM).

3.6. The practicability, reusability and stability

Other parameters (e.g., OVs-ZnO/Co$_3$O$_4$ loading, PMS dosage, pH, co-existing ions) showed trivial influence on the BPA removal in the OVs-ZnO/Co$_3$O$_4$/PMS system (Fig. S31 and Fig. 4**a**), indicating its wide pH operation range and good anti-interference toward complex water matrix. The concentration of inorganic anions was the maximum concentration of ions in some areas of Beijing surface water [69]. Furthermore, we investigated the effects of various inorganic anions and real water bodies on the OVs-ZnO/Co$_3$O$_4$/PMS/BA system. As shown in Fig. S32, the removal efficiency of BA reached 100% in the presence of H$_2$PO$_4^-$, NO$_3^-$ and SO$_4^{2-}$. Cl$^-$ and HCO$_3^-$ decreased the BA degradation efficiency, probably due to that Cl$^-$ and HCO$_3^-$ competed with BA to consume radicals (SO$_4^{•-}$ and $^•$OH) [63]. Due to the interference of various inorganic anions in tap water and lake water, the degradation efficiency of BA in these two real water bodies could only reach 45%.

Apart from BPA, OVs-ZnO/Co$_3$O$_4$/PMS system could also efficiently remove multiple refractory contaminants in wastewater, including SMX, CIP, PE, ATZ and BA, while some of these pollutants could not be removed completely in OVs-CoO$_x$/PMS system (Fig. 4**b**). This suggested that the As-OVs were more adaptable than the S-OVs. The reusability and stability of the OVs-ZnO/Co$_3$O$_4$ were also evaluated using the recovered catalyst for BPA removal. Fig. S33a showed that only a minimal decline (1.5%) was observed after five continuous cycles. Moreover, the XRD pattern of the used OVs-ZnO/Co$_3$O$_4$ matched perfectly with the fresh one, and the morphology experienced no significant change (Fig. S33b and **c**). The above results suggested that OVs-ZnO/Co$_3$O$_4$ had good stability and excellent durability for pollutant removal.

TOC removal efficiency is one of the important indicators to evaluate catalysts. As shown in Fig. S34, the TOC removal efficiency of OVs-ZnO/Co$_3$O$_4$ for removing BPA and BA reached 53.94% and 33.86% respectively after 1 min of reaction, proving that the OVs-ZnO/Co$_3$O$_4$/PMS system had a good water treatment efficiency.

The toxicity of BPA and BA solutions before and after the catalytic reaction was evaluated by the germination and growth process of mung beans [70,71]. It was observed from Fig. S35-S37 that the germination and growth of mung beans in both the degraded BPA and BA solutions by the OVs-ZnO/Co$_3$O$_4$ were similar with those in ultrapure water while significantly inhibited in the initial BPA and BA solutions. It could be
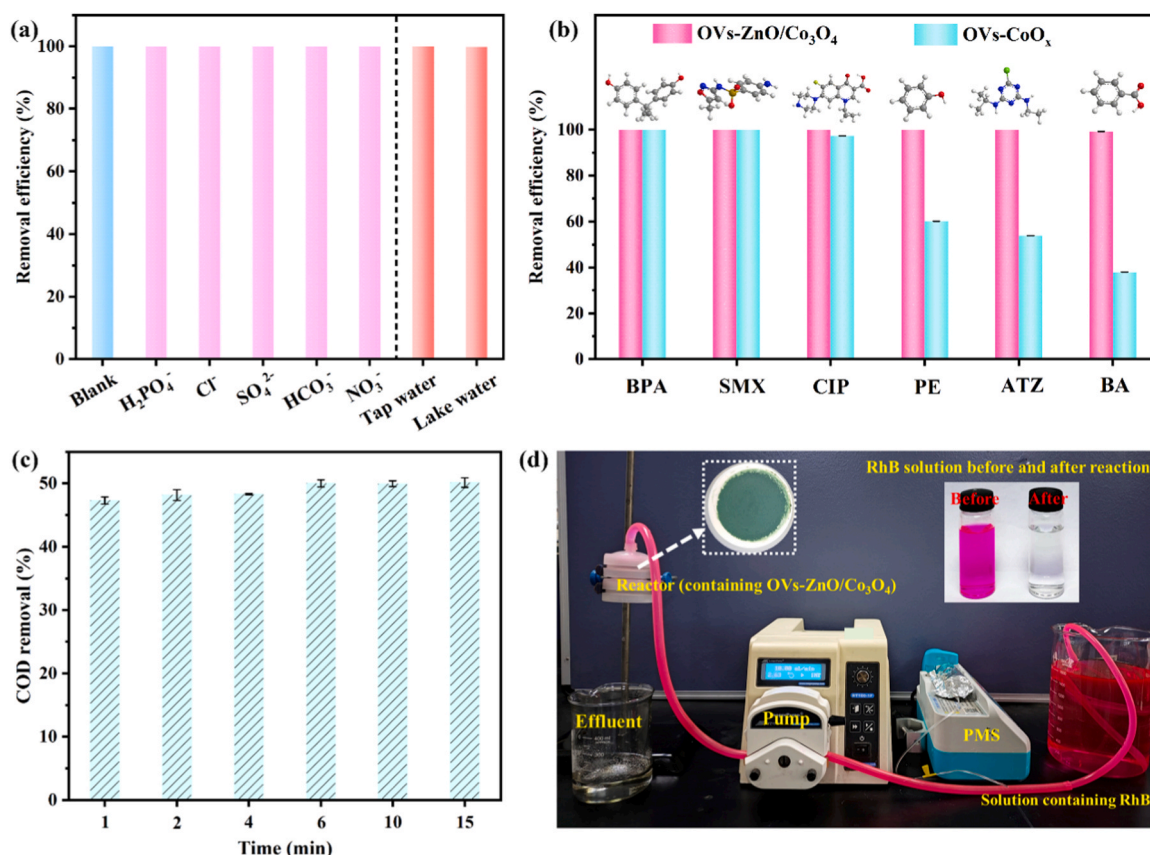
Fig. 4. (a) Effects of various inorganic anions and real water bodies on BPA removal. Reaction conditions: [OVs-ZnO/Co₃O₄] = 0.2 g/L, [PMS]₀ = 0.1 mM, BPA = 10 mg/L, H₂PO₄⁻ = 5.0 mg/L, Cl⁻ = 135.3 mg/L, SO₄²⁻ = 124.0 mg/L, HCO₃⁻ = 272 mg/L and NO₃⁻ = 13.6 mg/L. (b) Removal of different contaminants in the OVs-ZnO/Co₃O₄/PMS and OVs-CoOₓ/PMS system with 0.4 mM PMS. Reaction conditions: contaminants concentration = 10 mg/L, catalyst = 0.2 g/L, [PMS]₀ = 0.1 or 0.4 mM. (c) The COD removal efficiencies in OVs-ZnO/Co₃O₄/PMS/actual airport wastewater system. (d) Photograph of the wastewater treatment experiment equipment (RhB as indicator pollutant). Reaction conditions: [OVs-ZnO/Co₃O₄] = 100 mg, [PMS]₀ = 250 mM, [RhB]₀ = 10 mg/L, RhB pump flow rate = 10.0 mL/min and PMS pump flow rate = 0.3 mL/h.

concluded that the wastewater processed by the OVs-ZnO/Co₃O₄/PMS system favored the ecological security and compatibility.

As shown in Fig. 4c, OVs-ZnO/Co₃O₄ also presented good catalytic performance toward actual airport wastewater, and more than 50% COD removal was accomplished within 15 min under the condition of 0.8 g/L catalyst and 1.6 mM PMS. To further evaluate the actual application and visualize the catalytic capacity of the catalyst, a continuous operation reactor was built to remove RhB. As presented in Fig. 4d, the effluent became colorless after treatment by the OVs-ZnO/Co₃O₄ with a retention time of 60 s

4. Conclusion

Interfacial asymmetric oxygen vacancies (As-OVs) neighboring both Zn and Co (Zn⋯OVs⋯Co) were created in the OVs-ZnO/Co₃O₄ by glucose-assisted annealing strategy. The As-OVs in the OVs-ZnO/Co₃O₄ exhibited much better catalytic performance than the symmetric oxygen vacancies (S-OVs) in the OVs-CoOₓ. Noteworthy, these two OVs exhibited distinct catalytic behaviors for PMS activation. Specifically, PMS was easily adsorbed on the As-OVs to form PMS*, and then a rapid ETP regime occurred in the presence of BPA as an electron-rich contaminant. Interestingly, the PMS* tended to be decomposed into radicals once electron-poor BA replaced BPA due to the largely polarized PMS adsorbed by the unique asymmetric structures of As-OVs. Conversely, the symmetric site of S-OVs weakened the electron transfer from the catalyst to PMS, resulting in the difficult breakup of peroxide bond and production of radicals. Moreover, the OVs-ZnO/Co₃O₄ achieved good reusability, stability and anti-interference capacity

especially for the removal of electron-rich organics via a ETP regime. The actual airport wastewater could also be treated with more than 50% COD removal. This work refines the knowledge regarding the OVs-involved PMS-based AOPs in determining the oxidation pathways, clarifies the origin of the extremely different catalytic behaviors between the As-OVs and S-OVs, and highlights the distinctive dual-pathway oxidation behavior depending on the target contaminant. Based on the new findings, a controllable PMS-based AOP system with controlled oxidation pathways and on-demand selectivity will be established to effectively remove organic contaminants in a complex water matrix by constructing catalysts with As-OVs directionally.

CRediT authorship contribution statement

Zhao Chen: Resources, Supervision. **Wang Peng:** Resources. **Wang Chong-Chen:** Conceptualization, Funding acquisition, Project administration, Supervision, Writing – review & editing. **Liu Wen:** Resources. **Wang Fei:** Data curation, Methodology. **Fu Huifen:** Conceptualization, Funding acquisition, Project administration, Supervision, Writing – review & editing. **Meng Bingxin:** Methodology. **Wei Yuwei:** Software. **Liu Shan-Shan:** Data curation, Investigation, Software, Visualization, Writing – original draft.

Declaration of Competing Interest

The authors declare that they have no known competing financial interests or personal relationships that could have appeared to influence the work reported in this paper.

Data Availability

Data will be made available on request.

Acknowledgements

Appendix A. Supporting information

Supplementary data associated with this article can be found in the online version at doi:10.1016/j.apcatb.2024.123753.

References

[1] A. Alsbaiee, B.J. Smith, L. Xiao, Y. Ling, D.E. Helbling, W.R. Dichtel, Rapid removal of organic micropollutants from water by a porous β-cyclodextrin polymer, Nature 529 (2016) 190–194.
[2] R.P. Schwarzenbach, B.I. Escher, K. Fenner, T.B. Hofstetter, C.A. Johnson, U. Von Gunten, B. Wehrli, The challenge of micropollutants in aquatic systems, Science 313 (2006) 1072–1077.
[3] P.J. Alvarez, C.K. Chan, M. Elimelech, N.J. Halas, D. Villagrán, Emerging opportunities for nanotechnology to enhance water security, Nat. Nanotechnol. 13 (2018) 634–641.
[4] Y. Shang, X. Xu, B. Gao, S. Wang, X. Duan, Single-atom catalysis in advanced oxidation processes for environmental remediation, Chem. Soc. Rev. 50 (2021) 5281–5322.
[5] Y. Zhen, S. Zhu, Z. Sun, Y. Tian, Z. Li, C. Yang, J. Ma, Identifying the persistent free radicals (PFRs) formed as crucial metastable intermediates during peroxymonosulfate (PMS) activation by N-doped carbonaceous materials, Environ. Sci. Technol. 55 (2021) 9293–9304.
[6] Q. Zhou, C. Song, P. Wang, Z. Zhao, Y. Li, S. Zhan, Generating dual-active species by triple-atom sites through peroxymonosulfate activation for treating micropollutants in complex water, Proc. Natl. Acad. Sci. U. S. A. 120 (2023) e2300085120.
[7] W. Ren, G. Nie, P. Zhou, H. Zhang, X. Duan, S. Wang, The intrinsic nature of persulfate activation and N-doping in carbocatalysis, Environ. Sci. Technol. 54 (2020) 6438–6447.
[8] Y. Yao, C. Wang, X. Yan, H. Zhang, C. Xiao, J. Qi, Z. Zhu, Y. Zhou, X. Sun, X. Duan, J. Li, Rational regulation of Co-N-C coordination for high-efficiency generation of ¹O₂ toward nearly 100% selective degradation of organic pollutants, Environ. Sci. Technol. 56 (2022) 8833–8843.
[9] R. Huang, P. Gao, J. Zhu, Y. Zhang, Y. Chen, S. Huang, G. Wang, Z. Yu, S. Zhao, S. Zhou, Insights into the pollutant electron property inducing the transformation of peroxymonosulfate activation mechanisms on manganese dioxide, Appl. Catal. B 317 (2022) 121753.
[10] Z.Y. Guo, Y. Si, W.Q. Xia, F. Wang, H.Q. Liu, C. Yang, W.J. Zhang, W.W. Li, Electron delocalization triggers nonradical Fenton-like catalysis over spinel oxides, Proc. Natl. Acad. Sci. U. S. A 119 (2022) e2201607119.
[11] M. Yang, Z. Hou, X. Zhang, B. Gao, Y. Li, Y. Shang, Q. Yue, X. Duan, X. Xu, Unveiling the origins of selective oxidation in single-atom catalysis via Co-N₄-C intensified radical and nonradical pathways, Environ. Sci. Technol. 56 (2022) 11635–11645.
[12] J.C. Védrine, Heterogeneous catalysis on metal oxides, Catalysts 7 (2017) 341.
[13] J. Lee, U. Von Gunten, J.-H. Kim, Persulfate-based advanced oxidation: critical assessment of opportunities and roadblocks, Environ. Sci. Technol. 54 (2020) 3064–3081.
[14] H. Li, Z. Zhao, J. Qian, B. Pan, Are free radicals the primary reactive species in Co (II)-mediated activation of peroxymonosulfate? new evidence for the role of the Co (II)–peroxymonosulfate complex, Environ. Sci. Technol. 55 (2021) 6397–6406.
[15] X. Xie, Y. Li, Z.-Q. Liu, M. Haruta, W. Shen, Low-temperature oxidation of CO catalysed by Co₃O₄ nanorods, Nature 458 (2009) 746–749.
[16] C. Yang, S. Liu, Y. Wang, J. Song, G. Wang, S. Wang, Z.J. Zhao, R. Mu, J. Gong, The interplay between structure and product selectivity of CO₂ hydrogenation, Angew. Chem. Int. Ed. 58 (2019) 11242–11247.
[17] V. Iablokov, R. Barbosa, G. Pollefeyt, I. Van Driessche, S. Chenakin, N. Kruse, Catalytic CO oxidation over well-defined cobalt oxide nanoparticles: size-reactivity correlation, ACS Catal. 5 (2015) 5714–5718.
[18] Z. Xiao, Y.-C. Huang, C.-L. Dong, C. Xie, Z. Liu, S. Du, W. Chen, D. Yan, L. Tao, Z. Shu, Operando identification of the dynamic behavior of oxygen vacancy-rich Co₃O₄, Oxyg. Evol. React., J. Am. Chem. Soc. 142 (2020) 12087–12095.

[19] Y. Liu, Y. Peng, M. Naschitzki, S. Gewinner, W. Schöllkopf, H. Kuhlenbeck, R. Pentcheva, B. Roldan Cuenya, Surface oxygen vacancies on reduced Co₃O₄ (100): superoxide formation and ultra-low-temperature CO oxidation, Angew. Chem. Int. Ed. 60 (2021) 16514–16520.
[20] D. Liu, X. Xue, X. Zhang, Y. Huang, P. Feng, Highly efficient peroxymonosulfate activation by MOFs-derived oxygen vacancy-rich Co₃O₄/ZnO heterojunction nanocomposites to degrade pefloxacin, Sep. Purif. Technol. 305 (2023) 122451.
[21] C. Cheng, L. Chang, X. Zhang, Q. Deng, H. Chai, Y. Huang, Interface engineering-induced perovskite/spinel LaCoO₃/Co₃O₄ heterostructured nanocomposites for efficient peroxymonosulfate activation to degrade levofloxacin, Environ. Res (2023) 115994.
[22] J. Lim, Y. Yang, M.R. Hoffmann, Activation of peroxymonosulfate by oxygen vacancies-enriched cobalt-doped black TiO₂ nanotubes for the removal of organic pollutants, Environ. Sci. Technol. 53 (2019) 6972–6980.
[23] H. Li, J. Shang, Z. Yang, W. Shen, Z. Ai, L. Zhang, Oxygen vacancy associated surface Fenton chemistry: surface structure dependent hydroxyl radicals generation and substrate dependent reactivity, Environ. Sci. Technol. 51 (2017) 5685–5694.
[24] W. Wang, Y. Liu, Y. Yue, H. Wang, G. Cheng, C. Gao, C. Chen, Y. Ai, Z. Chen, X. Wang, The confined interlayer growth of ultrathin two-dimensional Fe₃O₄ nanosheets with enriched oxygen vacancies for peroxymonosulfate activation, ACS Catal. 11 (2021) 11256–11265.
[25] L. Wu, Z. Sun, Y. Zhen, S. Zhu, C. Yang, J. Lu, Y. Tian, D. Zhong, J. Ma, Oxygen vacancy-induced nonradical degradation of organics: critical trigger of oxygen (O₂) in the Fe–Co LDH/peroxymonosulfate system, Environ. Sci. Technol. 55 (2021) 15400–15411.
[26] K. Yu, L.L. Lou, S. Liu, W. Zhou, Asymmetric oxygen vacancies: the intrinsic redox active sites in metal oxide catalysts, Adv. Sci. 7 (2020) 1901970.
[27] J. Zhu, W. Shao, X. Li, X. Jiao, J. Zhu, Y. Sun, Y. Xie, Asymmetric triple-atom sites confined in ternary oxide enabling selective CO₂ photothermal reduction to acetate, J. Am. Chem. Soc. 143 (2021) 18233–18241.
[28] Z. Zhao, P. Wang, C. Song, T. Zhang, S. Zhan, Y. Li, Enhanced interfacial electron transfer by asymmetric Cu-Ov-in sites on In₂O₃ for efficient peroxymonosulfate activation, Angew. Chem. Int. Ed. 62 (2023) e202216403.
[29] C. Song, Q. Zhan, F. Liu, C. Wang, H. Li, X. Wang, X. Guo, Y. Cheng, W. Sun, L. Wang, J. Qian, B. Pan, Overturned loading of inert CeO₂ to active Co₃O₄ for unusually improved catalytic activity in fenton-like reactions, Angew. Chem. Int. Ed. 61 (2022) e202200406.
[30] J. Zhao, F. Li, H. Wei, H. Ai, L. Gu, J. Chen, L. Zhang, M. Chi, J. Zhai, Superior performance of ZnCoOₓ/peroxymonosulfate system for organic pollutants removal by enhancing singlet oxygen generation: The effect of oxygen vacancies, Chem. Eng. J. 409 (2021) 128150.
[31] D. Liu, X. Xue, X. Zhang, Y. Huang, P. Feng, Highly efficient peroxymonosulfate activation by MOFs-derived oxygen vacancy-rich Co₃O₄/ZnO pn heterojunction nanocomposites to degrade pefloxacin, Sep. Purif. Technol. 305 (2023) 122451.
[32] X. Xue, W. Liao, D. Liu, X. Zhang, Y. Huang, MgO/Co₃O₄ composite activated peroxymonosulfate for levofloxacin degradation: Role of surface hydroxyl and oxygen vacancies, Sep. Purif. Technol. 306 (2023) 122560.
[33] F. Wang, Y. Gao, S.-S. Liu, X.-H. Yi, C.-C. Wang, H. Fu, Fabrication strategies of metal–organic frameworks derivatives for catalytic aqueous pollutants elimination, Chem. Eng. J. 463 (2023) 142466.
[34] X.-W. Zhang, M.-Y. Lan, F. Wang, C.-C. Wang, P. Wang, C. Ge, W. Liu, Immobilized NC/Co derived from ZIF-67 as PS-AOP catalyst for effective tetracycline matrix elimination: from batch to continuous process, Chem. Eng. J. 450 (2022) 138082.
[35] D. Saliba, M. Ammar, M. Rammal, M. Al-Ghoul, M. Hmadeh, Crystal growth of ZIF-8, ZIF-67, and their mixed-metal, Deriv., J. Am. Chem. Soc. 140 (2018) 1812–1823.
[36] C. Xu, J. Tan, X. Zhang, Y. Huang, Petal-like CuCo₂O₄ spinel nanocatalyst with rich oxygen vacancies for efficient PMS activation to rapidly degrade pefloxacin, Sep. Purif. Technol. 291 (2022) 120933.
[37] Z. Cai, Y. Bi, E. Hu, W. Liu, N. Dwarica, Y. Tian, X. Li, Y. Kuang, Y. Li, X.Q. Yang, Single-crystalline ultrathin Co₃O₄ nanosheets with massive vacancy defects for enhanced electrocatalysis, Adv. Energy Mater. 8 (2018) 1701694.
[38] S. Zhan, H. Zhang, X. Mi, Y. Zhao, C. Hu, L. Lyu, Efficient fenton-like process for pollutant removal in electron-rich/poor reaction sites induced by surface oxygen vacancy over cobalt-zinc oxides, Environ. Sci. Technol. 54 (2020) 8333–8343.
[39] Y. Bu, H. Li, W. Yu, Y. Pan, L. Li, Y. Wang, L. Pu, J. Ding, G. Gao, B. Pan, Peroxydisulfate activation and singlet oxygen generation by oxygen vacancy for degradation of contaminants, Environ. Sci. Technol. 55 (2021) 2110–2120.
[40] H. Zhang, C. Li, L. Lyu, C. Hu, Surface oxygen vacancy inducing peroxymonosulfate activation through electron donation of pollutants over cobalt-zinc ferrite for water purification, Appl. Catal. B 270 (2020) 118874.
[41] A. Chen, X. Yu, Y. Zhou, S. Miao, Y. Li, S. Kuld, J. Sehested, J. Liu, T. Aoki, S. Hong, M.F. Camellone, S. Fabris, J. Ning, C. Jin, C. Yang, A. Nefedov, C. Wöll, Y. Wang, W. Shen, Structure of the catalytically active copper–ceria interfacial perimeter, Nat. Catal. 2 (2019) 334–341.
[42] Y. Yang, W. Si, Y. Peng, Y. Wang, H. Liu, Z. Su, J. Li, Defect engineering on CuMn₂O₄ spinel surface: a new path to high-performance oxidation catalysts, Environ. Sci. Technol. 56 (2022) 16249–16258.
[43] I. Moog, C. Feral-Martin, M. Duttine, A. Wattiaux, C. Prestipino, S. Figueroa, J. Majimel, A. Demourgues, Local organization of Fe³⁺ into nano-CeO₂ with controlled morphologies and its impact on reducibility properties, J. Mater. Chem. A 2 (2014) 20402–20414.
[44] S. Yamazaki, T. Matsui, T. Ohashi, Y. Arita, Defect structures in doped CeO₂ studied by using XAFS spectrometry, Solid State Ion. 136 (2000) 913–920.

[45] Y. Sun, Q. Liu, S. Gao, H. Cheng, F. Lei, Z. Sun, Y. Jiang, H. Su, S. Wei, Y. Xie, Pits confined in ultrathin cerium (IV) oxide for studying catalytic centers in carbon monoxide oxidation, Nat. Commun. 4 (2013) 2899.

[46] D. Zhang, Y. Li, P. Wang, J. Qu, Y. Li, S. Zhan, Dynamic active-site induced by host-guest interactions boost the Fenton-like reaction for organic wastewater treatment, Nat. Commun. 14 (2023) 3538.

[47] E.W. McFarland, H. Metiu, Catalysis by doped oxides, Chem. Rev. 113 (2013) 4391–4427.

[48] W. Ren, C. Cheng, P. Shao, X. Luo, H. Zhang, S. Wang, X. Duan, Origins of electron-transfer regime in persulfate-based nonradical oxidation processes, Environ. Sci. Technol. 56 (2022) 78–97.

[49] A. Du, H. Fu, P. Wang, C. Zhao, C.-C. Wang, Enhanced catalytic peroxymonosulfate activation for sulfonamide antibiotics degradation over the supported CoS_x-CuS_x derived from ZIF-L (Co) immobilized on copper foam, J. Hazard. Mater. 426 (2022) 128134.

[50] P. Neta, R.E. Huie, A.B. Ross, Rate constants for reactions of inorganic radicals in aqueous solution, J. Phys. Chem. Ref. Data 17 (1988) 1027–1284.

[51] S. Zhu, X. Li, J. Kang, X. Duan, S. Wang, Persulfate activation on crystallographic manganese oxides: mechanism of singlet oxygen evolution for nonradical selective degradation of aqueous contaminants, Environ. Sci. Technol. 53 (2018) 307–315.

[52] J. Miao, Y. Zhu, J. Lang, J. Zhang, S. Cheng, B. Zhou, L. Zhang, P.J. Alvarez, M. Long, Spin-state-dependent peroxymonosulfate activation of single-atom M–N moieties via a radical-free pathway, ACS Catal. 11 (2021) 9569–9577.

[53] X. Li, X. Wen, J. Lang, Y. Wei, J. Miao, X. Zhang, B. Zhou, M. Long, P.J. Alvarez, L. Zhang, CoN_1O_2 single-atom catalyst for efficient peroxymonosulfate activation and selective cobalt (IV)=O generation, Angew. Chem. Int. Ed. (2023) e202303267.

[54] X. Liu, P. Shao, S. Gao, Z. Bai, J. Tian, Benzoquinone-assisted heterogeneous activation of PMS on Fe_3S_4 via formation of active complexes to mediate electron transfer towards enhanced bisphenol A degradation, Water Res 226 (2022) 119218.

[55] Y. Zhou, J. Jiang, Y. Gao, J. Ma, S.-Y. Pang, J. Li, X.-T. Lu, L.-P. Yuan, Activation of peroxymonosulfate by benzoquinone: a novel nonradical oxidation process, Environ. Sci. Technol. 49 (2015) 12941–12950.

[56] Y. Zhou, S. Chen, H. Qie, S. Zhu, C. Zhang, X. Li, W. Wang, J. Ma, Z. Sun, Selective activation of peroxymonosulfate govern by B-site metal in delafossite for efficient pollutants degradation: Pivotal role of d orbital electronic configuration, Water Res 236 (2023) 119957.

[57] H. Zeng, X. Ling, H. Zhu, J. Deng, X. Ma, H. Zhang, L. Deng, Z. Shi, X. Li, Unraveling spongy Co_3O_4 mediated activation of peroxymonosulfate: Overlooked involvement of instantaneously produced high-valent-cobalt-oxo, Chemosphere 305 (2022) 135323.

[58] R. Luo, M. Li, C. Wang, M. Zhang, M.A. Nasir Khan, X. Sun, J. Shen, W. Han, L. Wang, J. Li, Singlet oxygen-dominated non-radical oxidation process for efficient degradation of bisphenol A under high salinity condition, Water Res 148 (2019) 416–424.

[59] W. Tan, W. Ren, C. Wang, Y. Fan, B. Deng, H. Lin, H. Zhang, Peroxymonosulfate activated with waste battery-based Mn-Fe oxides for pollutant removal: electron transfer mechanism, selective oxidation and LFER analysis, Chem. Eng. J. 394 (2020) 124864.

[60] L. Wang, J. Jiang, S.-Y. Pang, Y. Zhou, J. Li, S. Sun, Y. Gao, C. Jiang, Oxidation of bisphenol A by nonradical activation of peroxymonosulfate in the presence of amorphous manganese dioxide, Chem. Eng. J. 352 (2018) 1004–1013.

[61] P. Duan, J. Pan, W. Du, Q. Yue, B. Gao, X. Xu, Activation of peroxymonosulfate via mediated electron transfer mechanism on single-atom Fe catalyst for effective organic pollutants removal, Appl. Catal. B 299 (2021) 120714.

[62] F. Wang, Y. Gao, H. Fu, S.-S. Liu, Y. Wei, P. Wang, C. Zhao, J.-F. Wang, C.-C. Wang, Almost 100% electron transfer regime over Fe−Co dual-atom catalyst toward pollutants removal: Regulation of peroxymonosulfate adsorption mode, Appl. Catal. B 339 (2023) 123178.

[63] Y. Bao, Y. Lian, K. Huang, H. Yu, W. Liu, J. Zhang, M. Xing, Generating high-valent iron-oxo identical with $\equiv Fe^{IV}=O$ complexes in neutral microenvironments through peroxymonosulfate activation by Zn-Fe layered double hydroxides, Angew. Chem. Int. Ed. 61 (2022) e202209542.

[64] Y. Shi, X. Wang, X. Liu, C. Ling, W. Shen, L. Zhang, Visible light promoted Fe_3S_4 Fenton oxidation of atrazine, Appl. Catal. B 277 (2020) 119229.

[65] L. Kong, G. Fang, Z. Fang, Y. Zou, F. Zhu, D. Zhou, J. Zhan, Peroxymonosulfate activation by localized electrons of ZnO oxygen vacancies for contaminant degradation, Chem. Eng. J. 416 (2021) 128996.

[66] V. Shapovalov, H. Metiu, Catalysis by doped oxides: CO oxidation by $Au_xCe_{1-x}O_2$, J. Catal. 245 (2007) 205–214.

[67] X. Li, X. Huang, S. Xi, S. Miao, J. Ding, W. Cai, S. Liu, X. Yang, H. Yang, J. Gao, Single cobalt atoms anchored on porous N-doped graphene with dual reaction sites for efficient Fenton-like catalysis, J. Am. Chem. Soc. 140 (2018) 12469–12475.

[68] Y. Chen, G. Zhang, H. Liu, J. Qu, Confining free radicals in close vicinity to contaminants enables ultrafast fenton-like processes in the interspacing of MoS_2 membranes, Angew. Chem. Int. Ed. 58 (2019) 8134–8138.

[69] X.-H. Yi, H. Ji, C.-C. Wang, Y. Li, Y.-H. Li, C. Zhao, A. Wang, H. Fu, P. Wang, X. Zhao, Photocatalysis-activated SR-AOP over PDINH/MIL-88A (Fe) composites for boosted chloroquine phosphate degradation: Performance, mechanism, pathway and DFT calculations, Appl. Catal. B 293 (2021) 120229.

[70] X. Yuan, G. Geng, X. Liu, Z. Wang, Z. Wang, N.S. Shah, J. Song, Y. Guo, L. Kong, S. Liu, Cobalt and nitrogen co-doped monolithic carbon foam for ultrafast degradation of emerging organic pollutants via peroxymonosulfate activation, Ecotoxicol. Environ. Saf. 249 (2023) 114455.

[71] X. Yuan, Y. Leng, C. Fang, K. Gao, C. Liu, J. Song, Y. Guo, The synergistic effect of PMS activation by $LaCoO_3/g$-C_3N_4 for degradation of tetracycline hydrochloride: performance, mechanism and phytotoxicity evaluation, N. J. Chem. 46 (2022) 12217–12228.